Letter

Controlling magnetism and transport at perovskite cobaltite interfaces via strain-tuned oxygen vacancy ordering

Shameek Bose,[1] Manish Sharma,[1] Maria A. Torija,[1,2] Jeff Walter,[1,2] Nileena Nandakumaran,[1] John Dewey,[1] Josh Schmitt,[1] Jaume Gazquez,[3,*] Maria Varela,[4,*] M. Zhernenkov,[5] Michael R. Fitzsimmons,[5] Haile Ambaye,[6] Valeria Lauter,[6] Ondrej Hovorka,[7] Andreas Berger,[8] and Chris Leighton[1,†]

[1]*Department of Chemical Engineering and Materials Science, University of Minnesota, Minneapolis, Minnesota 55455, USA*
[2]*Recording Head Operations, Seagate Technology, Bloomington, Minnesota 55435, USA*
[3]*Institut de Ciencia de Materials de Barcelona (ICMAB-CSIC), Campus de la UAB, 08193 Bellaterra, Catalonia, Spain*
[4]*Departamento de Fisica de Materiales and Instituto Pluridisciplinar, Universidad Complutense de Madrid, Madrid 28040, Spain*
[5]*Los Alamos Neutron Science Center, Los Alamos National Laboratory, Los Alamos, New Mexico 87545, USA*
[6]*Neutron Scattering Division, Oak Ridge National Laboratory, Oak Ridge, Tennessee 37831, USA*
[7]*Faculty of Engineering and Physical Sciences, University of Southampton, Southampton SO17 1BJ, United Kingdom*
[8]*CIC nanoGUNE BRTA, 20018 Donostia-San Sebastian, Spain*

(Received 10 January 2025; accepted 4 March 2025; published 28 March 2025)

Complex oxides such as perovskite cobaltites exhibit rich phenomena at interfaces due to the complex interplay between their structural, defect, electronic, and magnetic degrees of freedom. We study this interplay here in the ferromagnetic metallic cobaltite $La_{1-x}Sr_xCoO_{3-\delta}$, using specific substrates to vary both the heteroepitaxial strain (compressive vs tensile) and growth orientation ((001) vs (110)). Transmission electron microscopy, electron energy-loss spectroscopy, high-resolution X-ray diffraction, magnetometry, polarized neutron reflectometry, and electronic magnetotransport measurements are applied. Lattice mismatch and growth orientation are found to enable the precise control of interfacial oxygen vacancy ordering in $La_{1-x}Sr_xCoO_{3-\delta}$, thus dictating strain relaxation and oxygen vacancy depth profiles, in turn controlling thickness-dependent magnetic and electronic properties. In particular, compressive strain and (110) orientations minimize deleterious magnetic/electronic dead layer effects, leading to the optimization of interfacial magnetism and transport. Strain and orientation tuning of oxygen vacancy ordering are thus established as powerful means to control physical properties at cobaltite-based interfaces, relevant to several fields.

DOI: 10.1103/PhysRevMaterials.9.L031402

Introduction. The properties of complex oxides such as perovskites are extraordinarily rich due to the complex interplay between their structural, electronic, and magnetic degrees of freedom [1–6]. This richness is further enhanced in perovskite oxide thin films, where surface effects, numerous interface effects, and effects of dimensional confinement emerge [1–6]. Perovskite cobaltites provide a classic example, particularly the archetypal $La_{1-x}Sr_xCoO_{3-\delta}$, which is of interest in many contexts, including electronic and magnetic properties [7,8], thermal properties [9,10], photonics [11], mixed ionic/electronic conduction [12], solid oxide fuel cells [13,14], and catalysis [15]. In bulk, this system evolves from the spin-state crossover insulator $LaCoO_3$ to the ferromagnetic (F) metal $SrCoO_3$ *via* a region of electronic/magnetic phase separation [7,8,16–21]. Spin-state polarons first form at low x in $La_{1-x}Sr_xCoO_{3-\delta}$ [16–18], followed by nanoscopic hole-rich F clusters at $x \approx 0.04$ [7,8,18–21], cluster percolation at $x \approx 0.18$ [7,8,21], and eventually a uniform F metallic state at $x > 0.22$ [7,8,21]. Epitaxial films of $La_{1-x}Sr_xCoO_{3-\delta}$ reveal further fascinating phenomena, including strain-controlled spin-states at low x ($LaCoO_3$ is F under tension, for example) [22–27], strain-tunable magnetocrystalline anisotropy (including perpendicular magnetic anisotropy (PMA) under compression) [28,29], and a giant form of anisotropic magnetoresistance (AMR) [30].

One particularly prominent feature of epitaxial $La_{1-x}Sr_xCoO_{3-\delta}$ films is their tendency toward not only oxygen vacancy (V_O) formation (particularly due to the instability of Co^{4+}), but also V_O order. Ordering of V_O is well known in *bulk* cobaltites, particularly $SrCoO_{3-\delta}$, where it leads to a series of low-symmetry ordered phases with $\delta = 0.25$, 0.33, 0.50, etc. [31–36]. These phases are exemplified by orthorhombic brownmillerite $SrCoO_{2.5}$, in which fully oxygenated octahedrally coordinated Co-O planes alternate with oxygen-deficient tetrahedral Co-O planes [31–36]. In *films* of $La_{1-x}Sr_xCoO_{3-\delta}$, however, local, short-range V_O order emerges even at low δ in the nominal perovskite phase [23,27,28,30,37,38]. This V_O ordering is commonly detected in transmission electron microscopy, but not in X-ray diffraction, underscoring the short-range nature of the order [23,27,28,30,37,38], on a length scale that has been tracked vs x [28]. This short-range V_O order is also fundamentally linked to strain [38]. Specifically, films

*Formerly at Materials Science and Engineering Division, Oak Ridge National Laboratory, Oak Ridge, Tennessee 37831, USA.
†Contact author: leighton@umn.edu

under tensile epitaxial strain tend to form V_O-ordered planes perpendicular to the substrate/film interface, whereas films under compressive strain form V_O ordered planes parallel to the interface [27,28,30,38]. This provides a novel mechanism of lattice mismatch accommodation in $La_{1-x}Sr_xCoO_{3-\delta}$, the expansion of interplanar spacing due to V_O order enabling tensile films to expand their in-plane lattice parameters and compressive films to expand out-of-plane lattice parameters [27,28,30,38]. Heteroepitaxial strain thus directly controls the V_O order in thin films of these materials [38].

This defect ordering significantly impacts electronic and magnetic properties and plays a key role in the strain-induced PMA [28,29] and giant AMR [30] exhibited by $La_{1-x}Sr_xCoO_{3-\delta}$ films. Magnetic/electronic dead layer effects [1–5,39–47] are also influenced by V_O order. In $SrTiO_3(001)/La_{1-x}Sr_xCoO_{3-\delta}$, for example, under tensile strain, F order and metallicity were found to rapidly decrease below a relatively large, x-dependent critical thickness t^* ($\sim$70 Å at $x = 0.50$) [47], eventually becoming entirely suppressed below a dead layer thickness t_d ($\sim$10-15 Å at $x = 0.50$). By detection of a characteristic intercluster magnetoresistance (MR) effect, and directly by small-angle neutron scattering, the property suppression below t^* was shown to be due to electronic/magnetic phase separation near the interface with the $SrTiO_3(001)$, i.e., breaking up of the uniform F state into nanoscopic F clusters within a non-F matrix [47]. Scanning transmission electron microscopy with electron energy-loss spectroscopy (STEM-EELS) was used to link the magnetic phase separation to depletion of the hole density near the interface with $SrTiO_3(001)$, driven directly by V_O accumulation related to the strain-induced V_O order [47]. In $SrTiO_3(001)/La_{1-x}Sr_xCoO_{3-\delta}$, magnetic/electronic dead layer effects are thus heavily chemically influenced, ultimately being dictated by strain-induced V_O formation and ordering.

The above situation creates a clear opportunity, which is the focus of this Letter. Specifically, with the magnetic/electronic dead layer effects at $La_{1-x}Sr_xCoO_{3-\delta}$ interfaces known to be directly linked to V_O formation and ordering [47], and the V_O order known to be tunable *via* strain [27,28,30,38], control of heteroepitaxial strain could provide a means to fine-tune and mitigate dead layer effects. We investigate this hypothesis by studying primarily $La_{0.5}Sr_{0.5}CoO_{3-\delta}$ (LSCO) films grown on $SrTiO_3(001)$, $SrTiO_3(110)$, and $LaAlO_3(001)$ substrates, covering both tensile and compressive strain, and two growth orientations. STEM-EELS, high-resolution X-ray diffraction, magnetometry, polarized neutron reflectometry (PNR), and electronic transport and MR measurements reveal that lattice mismatch and orientation indeed control the V_O order, and thus oxygen depth profiles. Magnetic and electronic properties are profoundly affected in turn. In particular, compressive strain and (110) orientations minimize interfacial electronic/magnetic phase separation in LSCO, enabling mitigation of dead layer effects and optimization of thin-film properties. Strain-tuned oxygen defect ordering is thus established as a powerful means to control physical properties at cobaltite-based interfaces, with implications across several fields.

Methods. A full description of methods used for deposition, characterization, measurement, and analysis is provided in Supplemental Material Section A [48]. Briefly, the majority of the $x = 0.5$ LSCO films were sputter-deposited at 700 °C in 28 mTorr of O_2 and 42 mTorr of Ar, as in Refs. [38,47,49]. For comparison, a small number of films were deposited by high-pressure-oxygen sputtering, at 600 °C in 1.3 Torr of pure O_2, as in Refs. [27,28,30]. As noted and discussed below, for PNR measurements, $x = 0.3$ films were studied. High-resolution x-ray diffraction, including specular diffraction, rocking curves, and in-plane diffraction, was performed on a Panalytical X'Pert Pro. STEM-EELS measurements were carried out at 100 kV in a VG Microscopes HB501UX and a Nion UltraSTEM100 equipped with Nion aberration correctors and Gatan Enfina EEL spectrometers; details are in Supplemental Material Section A [48]. Magnetometry was performed in a Quantum Design MPMS-XL, from 10–300 K, in fields up to 70 kOe. A method described in Supplemental Material Section A [48] was used to extract T_C distributions from such data. Magnetotransport measurements used Mg(5 nm)/Au(50 nm) contacts in a van der Pauw geometry, both AC resistance bridge and DC methods, and a Janis cryostat with a 1.5-K base temperature and 90-kOe magnet. PNR was done at Los Alamos National Laboratory and at the Spallation Neutron Source at Oak Ridge National Laboratory. Data were acquired at 5–10 K in a 10-kOe magnetic field in the film plane; further details (including refinement methods) are provided in Supplemental Material Sections A and B [48]. As noted above, for PNR, the composition $La_{0.7}Sr_{0.3}CoO_{3-\delta}$ was studied, i.e., $x = 0.3$ rather than $x = 0.5$. This was done to facilitate the detection and quantification of dead layer effects, which grow with decreasing x in $La_{1-x}Sr_xCoO_{3-\delta}$ [47].

Results and Analysis. As shown in Supplemental Material Fig. S1 [48], specular and in-plane high-resolution x-ray diffraction data confirm high-quality, phase-pure, smooth, epitaxial LSCO films on all substrates. This is confirmed by the Z-contrast cross-sectional STEM images in Figs. 1(a)–1(c), which additionally reveal clear signatures of V_O order. In prior STEM/EELS work, the stripe features in such images were definitively assigned to V_O order in the LSCO [47,50]. Of highest importance here, the V_O ordering indeed switches from perpendicular to the interface under 1.8% tensile mismatch on $SrTiO_3(001)$ [Fig. 1(a)], to parallel to the interface under -1.2% compressive mismatch on $LaAlO_3(001)$ [Fig. 1(c)] [28,30,38]. Consistent with brownmillerite-like ordering [28–38], the V_O-ordered planes on $SrTiO_3(110)$ then take diagonal orientations [Fig. 1(b)] [38]. Prior work established that these V_O ordering orientations profoundly impact thickness- and depth-dependent strain relaxation in such LSCO films [38]. In particular, compressive strain on $LaAlO_3(001)$, and the multi-domain diagonal V_O-ordering on $SrTiO_3(110)$, were found to accelerate strain relaxation with increasing thickness [38].

Figures 1(d)–1(f) shows that the mismatch-controlled V_O ordering orientation also impacts the chemical composition in the z direction (perpendicular to the substrate/film interface), specifically the oxygen concentration. Note that STEM/EELS quantifies oxygen concentration with good relative uncertainty (the error bars on the plots) but much larger absolute uncertainty (see figure caption), and so we interpret only relative variations. The prominent feature in Fig. 1(d) is the pronounced fall-off in oxygen content in the LSCO on approaching the interface ($z = 0$) with $SrTiO_3(001)$, under

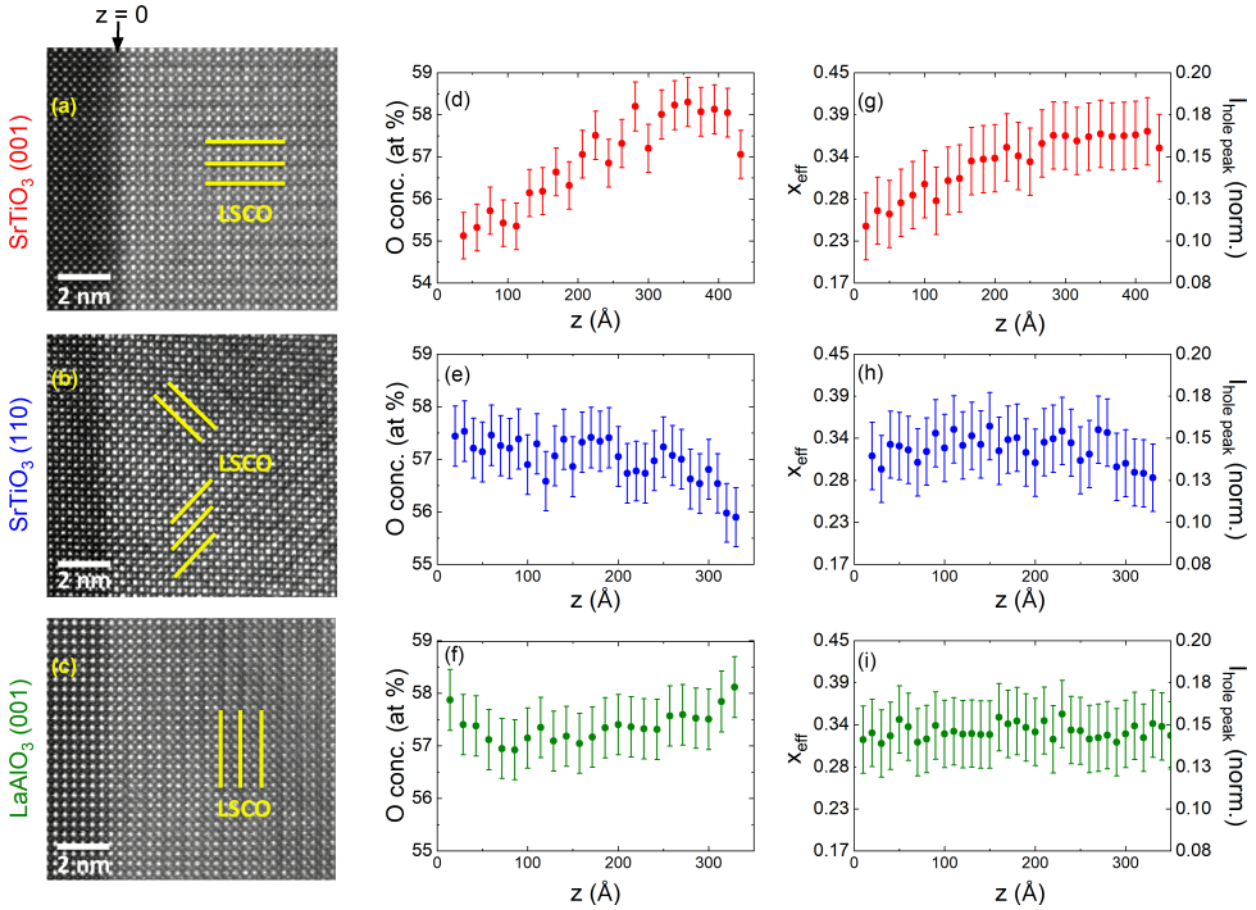

FIG. 1. (a)–(c) Atomic-resolution Z-contrast STEM images of 350 to 450-Å-thick LSCO films on $SrTiO_3$(001), $SrTiO_3$(110) ([001] pseudocubic zone axis), and $LaAlO_3$(001) substrates. The yellow lines highlight the local V_O ordering orientations. (d)–(f) Corresponding z profiles [see (a) for the definition of $z = 0$ (the substrate/film interface)] of the O content in the LSCO from EELS data. (g)–(i) Corresponding z profiles of x_{eff} (left axis, from the calibration of Torija *et al.* [47]) and the EELS hole peak intensity (right axis). The error bars in (d)–(i) are *relative* errors; the *absolute* error is ∼5 at.% on O content and ∼0.1 on x_{eff}. Data in (a), (d), (g) adapted from Ref. [47].

tensile strain, as mentioned above [45]. Remarkably, this undesirable oxygen depth profile is alleviated not only under compressive strain [Fig. 1(f)], but also on the same $SrTiO_3$ substrates but in the (110) [Fig. 1(e)] orientation. Figures 1(g)–1(i) then shows corresponding depth profiles of the normalized EELS intensity at the ∼527-eV pre-peak to the O K edge, which is known to reflect the hole doping density in LSCO [47], in addition to the Co ions spin state [50]. The right axes in Figs. 1(g)–1(i) show this intensity, while the left axes show the conversion to effective doping, x_{eff}, using the calibration of Torija *et al.* [47]. Consistent with the oxygen depth profiles in Figs. 1(d)–1(f), the hole depth profiles in Figs. 1(g)–1(i) show the hole depletion at the LSCO/substrate interface discussed above [47] only in the $SrTiO_3$(001) case [Fig. 1(g)], replaced by remarkably uniform hole depth profiles on $SrTiO_3$(110) [Fig. 1(h)] and $LaAlO_3$(001) [Fig. 1(i)]. The lattice mismatch and growth orientation thus precisely control not only the V_O order orientation in LSCO films, but also the depth profiles of the oxygen content and x_{eff}, further underscoring the deep connections between V_O formation, V_O order, and strain in this system [38]. We emphasize that all $La_{0.5}Sr_{0.5}CoO_{3-\delta}$ films here are oxygen-deficient to some degree, but Figs. 1(d)–1(f) shows that on $SrTiO_3$(001) additional V_O accumulate near the interface, but not on $SrTiO_3$(110) or $LaAlO_3$(001). This is very likely related to the trends in strain relaxation discussed in Ref. [38], particularly the more efficient strain relaxation in the (110) orientation, where V_O-ordered planes form at ∼45° to the interface [Fig. 1(b)].

With very different oxygen and hole doping depth profiles established on $SrTiO_3$(001), $SrTiO_3$(110), and $LaAlO_3$(001), magnetic properties of these LSCO films are detailed in Fig. 2. Figures 2(a)–2(c) are magnetization (M) vs temperature (T) curves at multiple thickness (t), all measured (and cooled) in an in-plane applied magnetic field (H) of 1 kOe. On $SrTiO_3$(001) [Fig. 2(a)], the thick-film behavior is as expected, the Curie temperature (T_C) being ∼225 K and the magnetization in this (non-saturating) field reaching well over 1 μ_B/Co, comparable to bulk [7,8]. As t is decreased, however, both T_C and $M(T \quad 0)$ are reduced, first moderately down to ∼70 Å [∼18 unit cells (u.c.)] then rapidly below this. By $t = 30$ Å (∼8 u.c.), barely any signature of F order remains, consistent with Torija *et al.* [47], pointing to substantial t^*. On the same substrate ($SrTiO_3$) but simply in a different orientation ((110)), Fig. 2(b) reveals that dead layer effects are clearly reduced. The drops in T_C and $M(T \quad 0)$ are more gradual, resulting in retention of substantial M and a significant T_C (∼ 150 K) even at $t = 30$ Å (∼ 8 u.c.). On $LaAlO_3$(001) [Fig. 2(c)], the situation is complicated by the

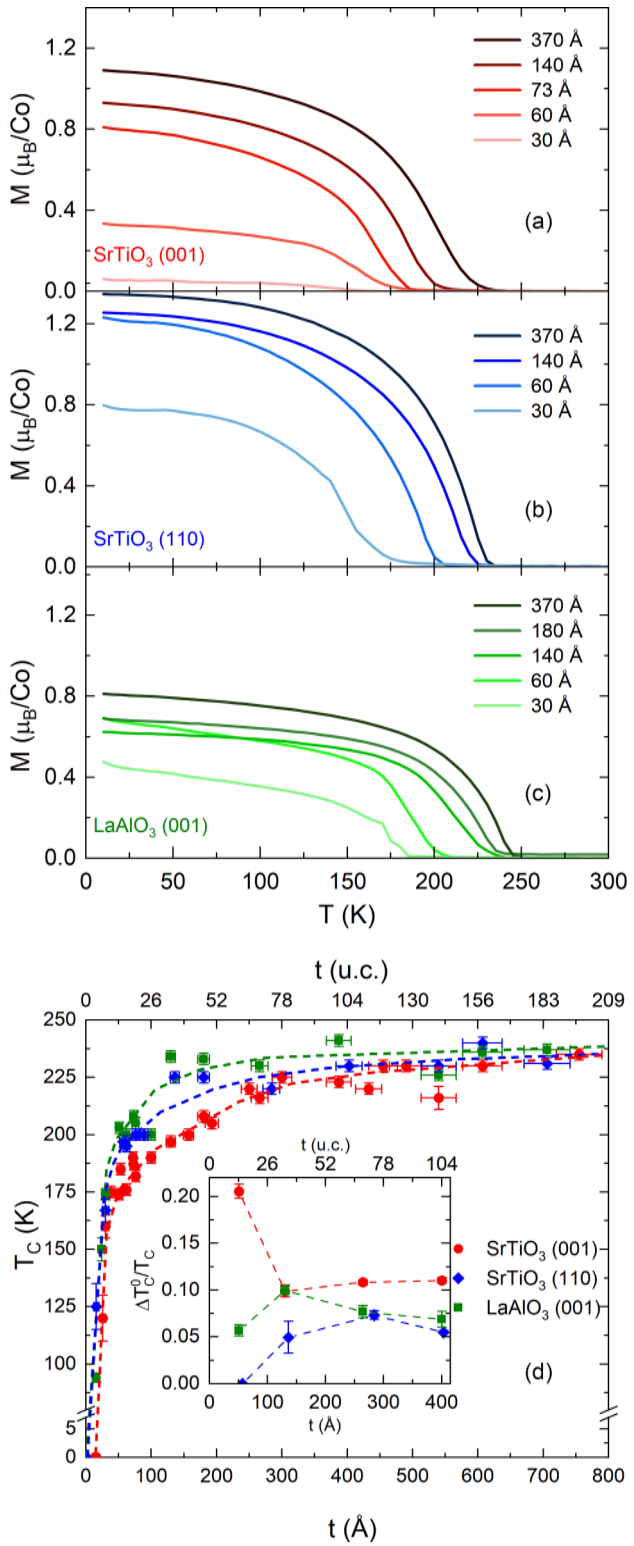

FIG. 2. (a)–(c) $M(T)$ at various t for LSCO films on (a) $SrTiO_3(001)$, (b) $SrTiO_3(110)$, and (c) $LaAlO_3(001)$. Data were taken after field cooling and measuring in 1 kOe. (d) $T_C(t)$ for LSCO films on $SrTiO_3(001)$, $SrTiO_3(110)$, and $LaAlO_3(001)$; dotted lines are guides to the eye. Inset: Corresponding T_C^0/T_C vs t from the analysis described in the text; the error bars correspond to uncertainties from the regression analysis described in Supplemental Material Section A [48]. Red data in the main panel of (d) adapted from Ref. [47].

tendency toward PMA [28], which results in lower M for in-plane measurements. Nevertheless, the suppression of F order with decreasing t is clearly more similar to $SrTiO_3(110)$ than $SrTiO_3(001)$, resulting in preservation of strong F order with T_C as high as ∼175 K at $t = 30$ Å (∼8 u.c.). The full $T_C(t)$ from a larger set of measurements is shown in Fig. 2(d), revealing consistency with both Figs. 2(a)–2(c) and 1. On all three substrates, the T_C suppression is gradual down to some thickness, below which T_C drops quickly. The $T_C(t)$ curves are distinctly shifted, however (note the very low t behavior in particular), with the $SrTiO_3(001)$ case indicating the highest t_d, followed by $SrTiO_3(110)$, then $LaAlO_3(001)$. Consistent with the oxygen/hole profiling in Fig. 1, tensile strain thus results in the highest t^* and t_d in LSCO, but this can be mitigated in the (110) vs (001) orientation, while compressive strain minimizes dead layer effects.

Further insight was obtained from quantitative analysis of $M(T)$. As described in Supplemental Material Section A [48], the method of Campillo *et al.* [51] and Berger *et al.* [52] was used to extract the width of the intrinsic T_C distribution (T_C^0) of these LSCO films. This is shown in the inset to Fig. 2(d) as a function of t, normalized to T_C, on all three substrates. For LSCO on $LaAlO_3(001)$ and $SrTiO_3(110)$, T_C^0/T_C is seen to be relatively low, below ∼7.5% in almost all cases. On $SrTiO_3(001)$, however, even in the thick-film limit, T_C^0/T_C exceeds 10%, rising sharply to >20% below ∼100 Å (∼26 u.c.). Consistent with the overall picture of much larger t^* in $SrTiO_3(001)$/LSCO films due to an extended region of interfacial magnetic phase separation [47], this suggests substantial magnetic inhomogeneity, likely depth-wise, which we now probe *via* PNR.

Figures 3(a)–3(c) shows neutron reflectivity (R) vs wave vector transfer (q) in the ++ and −− channels, from 400 to 450-Å-thick $La_{0.7}Sr_{0.3}CoO_{3-\delta}$ films on all three substrates, the insets showing the respective spin asymmetry, $(R^{++} - R^{--})/(R^{++} + R^{--})$. (The plus/minus signs here denote neutrons with spin parallel/antiparallel to the applied field, before and after reflection; the two channels measured are therefore non-neutron-spin-flip (see Supplemental Material Section A for details [48])). In these $T = 5 - 10$ K, $H = 10$ kOe data, thickness fringes are observed in all cases, along with clear splittings between $R^{++}(q)$ and $R^{--}(q)$, but with quantitatively different q dependencies. This is seen most clearly in the insets to Figs. 3(a)–3(c), where the dampening of the spin asymmetry oscillations with increasing q is quite different on $SrTiO_3(001)$ compared to $SrTiO_3(110)$ and $LaAlO_3(001)$.

Shown in Figs. 3(d)–3(f) are z profiles of the nuclear scattering length density (SLD) on the left axes and magnetic SLD on the right axes, as extracted from PNR refinements described in detail in Supplemental Material Section A, Fig. S2, and Table S1 [48]. Briefly, GenX [53] refinements [solid lines in Figs. 3(a)–3(c)] were performed by breaking the LSCO into multiple layers with distinct nuclear and magnetic SLDs and roughnesses. In the $SrTiO_3(001)$/LSCO case, four layers were necessary to satisfactorily refine the data, capturing suppressed nuclear and magnetic SLD at both the surface and interface (see Table S1 and Fig. S2 [48]). This is shown in Fig. 3(d), where the most striking features are the modest (∼15%) suppression of nuclear SLD on approaching the film/substrate interface, accompanied by

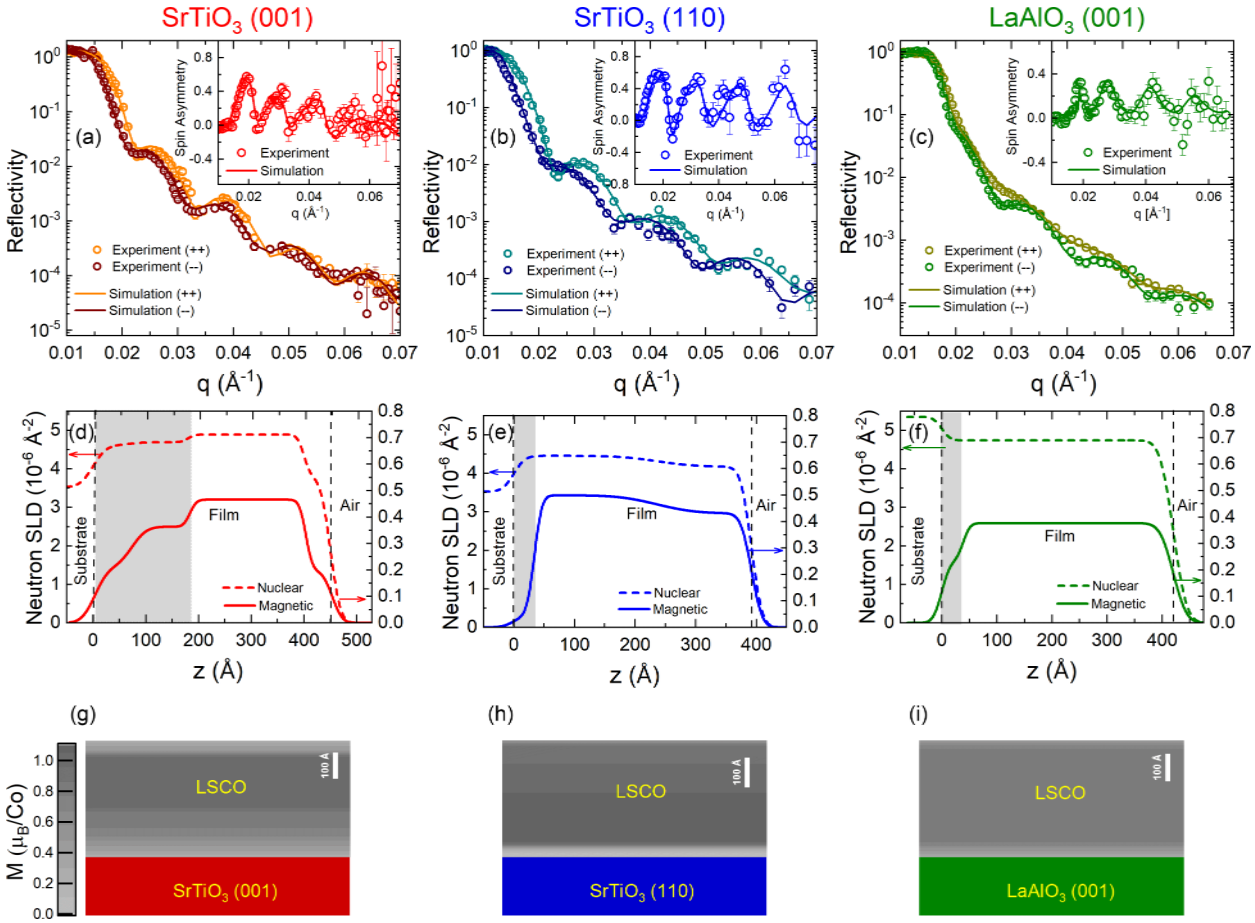

FIG. 3. (a)–(c) 5-10-K non-neutron-spin-flip (++ and −−) polarized neutron reflectivity vs q for 400 to 450-Å-thick $La_{0.7}Sr_{0.3}CoO_{3-\delta}$ films on (a) $SrTiO_3$(001), (b) $SrTiO_3$(110), and (c) $LaAlO_3$(001) substrates; both data (where the error bars are standard deviations) and fits are shown. All data were taken in an in-plane applied magnetic field of 10 kOe, after cooling in the same field. Insets: Corresponding spin asymmetry vs q. (d)–(f) Corresponding extracted z profiles of the nuclear (dashed line, left axes) and magnetic (solid line, right axes) SLD; both the left and right axes are SLDs, in the same units. The gray bands here mark the regions with suppressed magnetization, in accord with panel (g)–(i) and S2, and Table S1. (g)–(i) Corresponding grayscale schematics of the magnetization depth profile [scale shown in (g)]. For the $LaAlO_3$ case only (see Supplemental Material Section A [48]), R^+ and R^- were measured, with no polarization analysis.

strong (∼70%) suppression of the magnetic SLD. As the nuclear SLD of $La_{1-x}Sr_xCoO_{3-\delta}$ decreases with increasing δ [54], we interpret the nuclear SLD suppression in terms of a reduction in oxygen concentration on approaching the $SrTiO_3$(001) interface, consistent with the STEM-EELS in Fig. 1(d). The accompanying strong suppression of the magnetic SLD then reflects the substantial t^* on this substrate, consistent with Figs. 2(a) and 2(d). The interfacial region with suppressed magnetic SLD [gray band in Fig. 3(d)] in fact spans ∼180 Å in this $SrTiO_3$(001)/$La_{0.7}Sr_{0.3}CoO_{3-\delta}$ case, in very good agreement with the t^* deduced by Torija *et al.* at this x [47], which is just over two times the equivalent at $x = 0.50$. Also consistent with Figs. 1 and 2, Figs. 3(e) and 3(f) shows that this interfacial region with suppressed magnetic SLD shrinks dramatically on both $SrTiO_3$(110) and $LaAlO_3$(001), to only 30 − 40 Å (8-10 u.c.), even at $x = 0.3$. Figures 3(g)–3(i) summarize the key findings from PNR, converting the magnetic SLD to magnetization and depicting the depth profiles pictorially. The suppressed-magnetization interfacial region shrinks strikingly from the $SrTiO_3$(001) case to the $SrTiO_3$(110) and $LaAlO_3$(001) cases, confirming that the suppressed magnetism with decreasing t in Figs. 2(a)–2(d) reflects magnetic dead layer effects, consistent with the inset to Fig. 2(d). Note that the lower magnetization in the interior of the $LaAlO_3$(001)/$La_{0.7}Sr_{0.3}CoO_{3-\delta}$ film is simply due to compression-induced PMA [28,29], which is not entirely overcome in this 10-kOe in-plane field.

Dead layer effects of course also manifest in electronic transport. This is considered in Fig. 4, which shows resistivity (ρ) vs T for LSCO films on $SrTiO_3$(001) (top panels), $SrTiO_3$(110) (middle panels), and $LaAlO_3$(001) (bottom panels), at various illustrative t (from 130 Å on the left to 30 Å on the right). Considering $SrTiO_3$(001)/LSCO first, Fig. 4(a) shows the expected behavior in the relatively thick-film (130-Å) limit, i.e., metallic transport with $d\rho/dT > 0$ both above and below T_C (∼ 200 K from the inflection point, in agreement with Fig. 2(d)) [7,8,28,30,47,49]. The 300-K and residual resistivities are 0.47 and 0.16 mΩcm, respectively, comparable to other reports of high-quality LSCO films [28,30,47,49]. Decreasing t just to 60 Å (∼ 16 u.c.), however, increases ρ(300 K) to 0.61 mΩ cm; $\rho(T)$ still reflects T_C at this thickness but with an overall

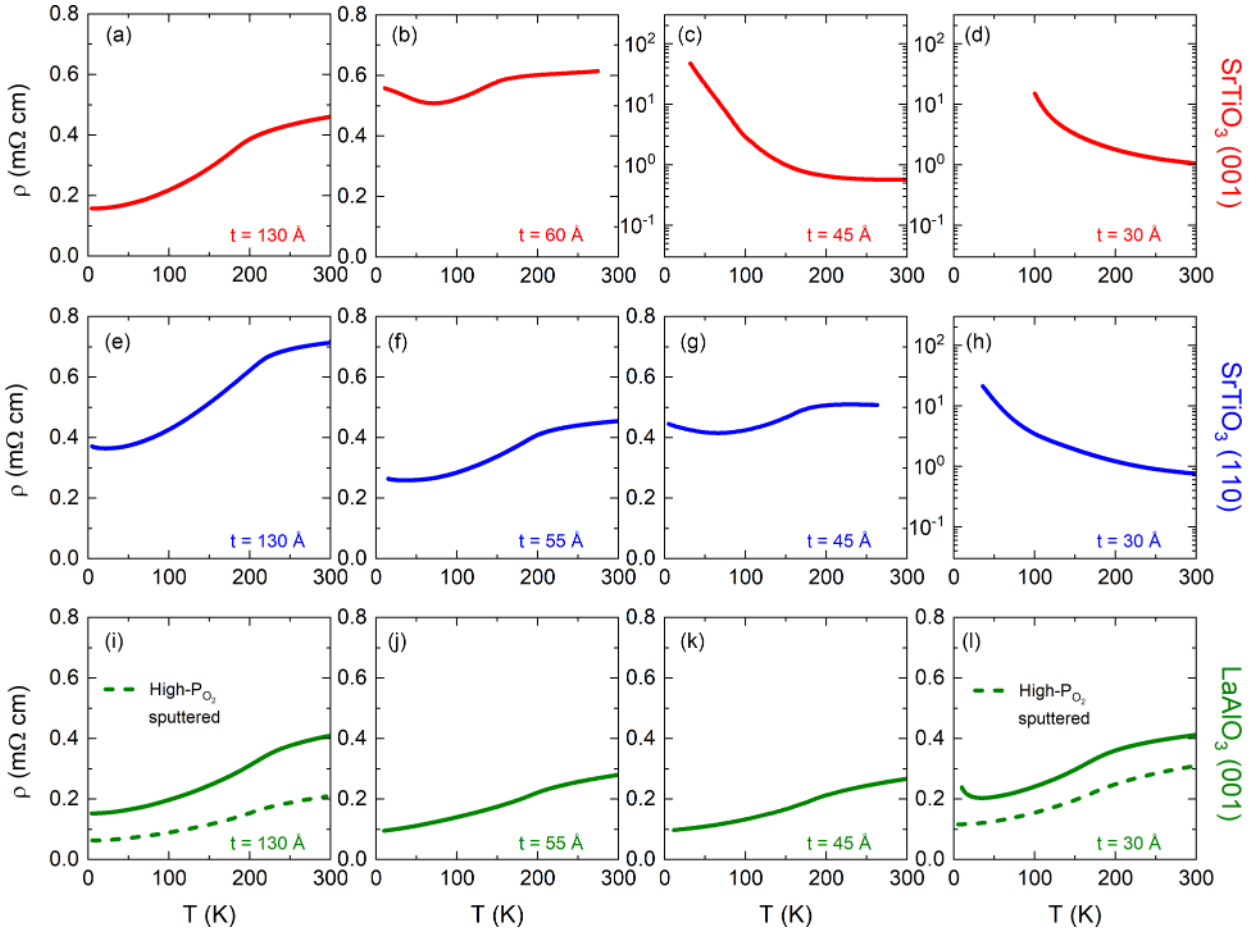

FIG. 4. $\rho(T)$ for LSCO films with $t = 130$ Å, $55 - 60$ Å, 45 Å, and 30 Å (from left to right) on $SrTiO_3(001)$ [top, (a)–(d)], $SrTiO_3(110)$ [middle, (e)–(h)], and $LaAlO_3(001)$ [bottom, (i)–(l)] substrates. Data on $SrTiO_3(110)$ are averaged between the [001] and [−110] in-plane directions, which showed minor anisotropy. In (i), (l), the dashed lines show equivalent data from high-pressure-oxygen-sputtered films.

barely metallic form. Decreasing t further to 45 Å (∼12 u.c.) results in insulating $\rho(T)$, becoming strongly insulating by 30 Å (∼8 u.c.). Figures 4(a)–4(d) thus show strong degradation of transport properties below $t^* \approx$ 60-70 Å (∼18 u.c.) in LSCO on $SrTiO_3(001)$ [47], consistent with the magnetism suppression in Figs. 2(a) and 2(d).

Distinctly different behavior occurs on $SrTiO_3(110)$, where Figs. 4(e)–4(h) reveals predominantly metalliclike behavior ($d\rho/dT > 0$) down to 45 Å (∼12 u.c.), followed by only weakly insulating behavior at 30 Å (∼8 u.c.). Again consistent with magnetic trends, suppression of metallicity thus does not occur in the $SrTiO_3(110)$/LSCO case until below ∼10 u.c. Under mild compressive strain on the other hand, on $LaAlO_3(001)$, Figs. 4(i)–4(l) reveals preservation of metallicity down to even 30 Å thickness, with only a small low-T upturn in $\rho(T)$, indicating an electronic dead layer well below 8 unit cells. While the vast majority of LSCO films studied in this work were deposited by conventional reactive sputtering at moderate oxygen pressure (28 mTorr) [38,47,49], Figs. 4(i) and 4(l) also shows some results from high-pressure-oxygen sputtering (at ∼1.3 Torr) [27,28,30,54]. This deposition technique generates some of the lowest residual resistivities reported for LSCO [30], reaching 0.07 mΩ cm at 130 Å and 0.10 mΩcm even in the very thin-film limit at 30 Å (∼8 u.c). (Such films also have slightly improved magnetic properties, including $T_C \approx 195$ K at $t = 30$ Å (compare to Fig. 2(c))). Clearly, the trends in magnetism in Figs. 2 and 3 are also reflected in the transport data in Fig. 4, the very high sensitivity of the resistivity to dead layer effects [1–5,39–47] even distinguishing the behavior on $SrTiO_3(110)$ and $LaAlO_3(001)$, the latter generating the lowest t^* and t_d. As a final comment on Fig. 4, we note that on some substrates [e.g., $LaAlO_3(001)$] a slightly nonmonotonic thickness dependence arises, where the resistivity marginally increases at the highest thicknesses [compare Figs. 4(i) and 4(j), for example]. This is very likely related to strain relaxation (and accompanying surface roughening), as high-pressure-sputtered films, which exhibit larger critical thickness for strain relaxation, exhibit no such nonmonotonicity [30].

As alluded to in the introduction, in $SrTiO_3(001)$/LSCO, MR measurements played a key role in the deduction that electronic/magnetic phase separation underpins the prominent dead layer effects [47]. Figure 5 thus shows low-T (10-K) MR(H) data for LSCO films at an illustrative thickness of 60 Å on (a) $SrTiO_3(001)$, (b) $SrTiO_3(110)$, and (c) $LaAlO_3(001)$. As illustrated in the schematics in (d)–(f), these data were taken in in-plane H, both parallel [top panels in (a)–(c)] and perpendicular [bottom panels in (a)–(c)] to the current (I). The $SrTiO_3(001)$/LSCO case [Fig. 5(a)] is as reported by Torija *et al.* [47], displaying negative MR that is hysteretic

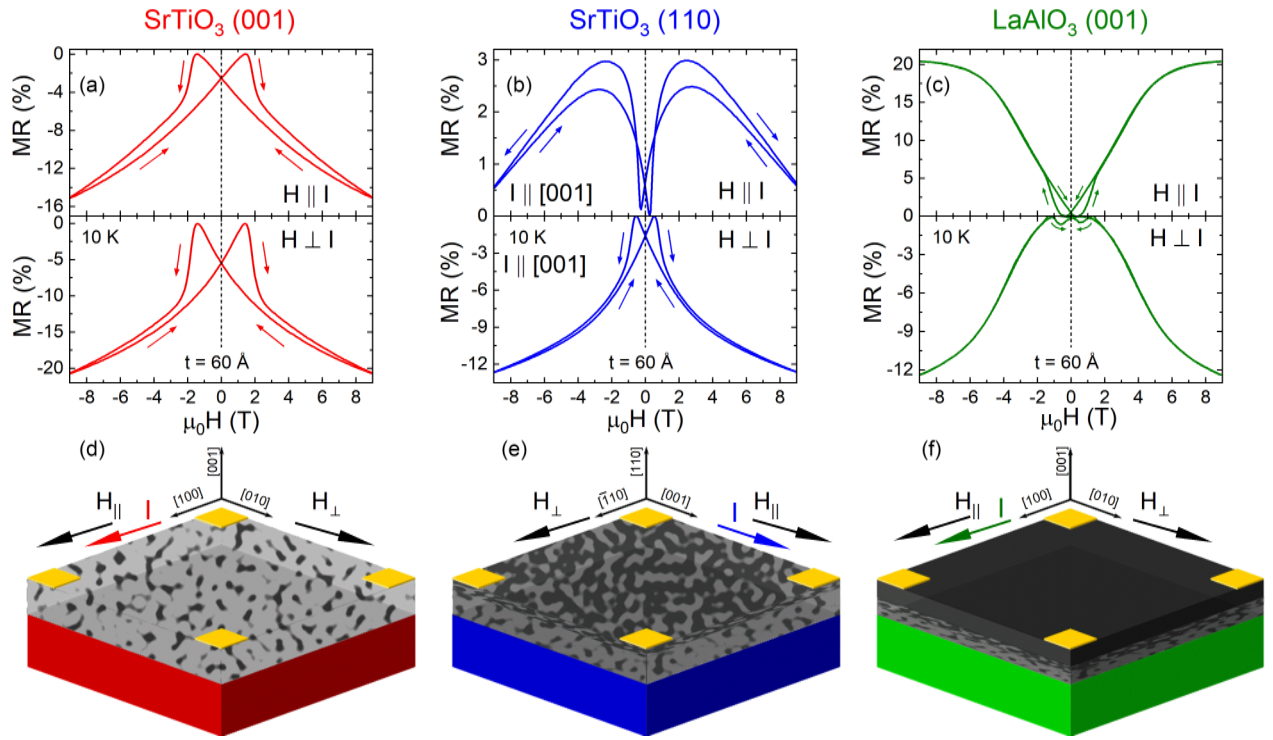

FIG. 5. (a)–(c) 10-K MR(H) for 60-Å-thick LSCO films on (a) $SrTiO_3$(001), (b) $SrTiO_3$(110), and (c) $LaAlO_3$(001) substrates. H is in the film plane and data are shown for in-plane I both parallel (top) and perpendicular (bottom) to H [see the schematics in (d)–(f)]. (d)–(f) Corresponding schematics where dark regions are ferromagnetic and metallic and lighter regions are non-ferromagnetic and insulating; gold squares are contacts. MR is defined as $[\rho(H) - \rho(H_c)]/\rho(H_c)$, where H_c is the coercive field.

in nature (peaking at the coercive fields) and almost entirely isotropic. These are the classic signatures of the intercluster MR originally discovered in magnetically phase-separated low-x bulk $La_{1-x}Sr_xCoO_{3-\delta}$ single crystals [18,21], then later in $SrTiO_3$(001)/$La_{0.5}Sr_{0.5}CoO_{3-\delta}$ films with $t < t^*$ [47,49]. This implicates the scenario depicted schematically in Fig. 5(d), where nonpercolated metallic F clusters exist within a non-F insulating matrix (because $t < t^*$), resulting in intercluster MR [Fig. 5(a)] and insulating transport [Figs. 4(b)–4(d)] [47,55].

The situation is very different on $LaAlO_3$(001), as shown in Fig. 5(c). In this case, the near-isotropic, hysteretic, negative MR of Fig. 5(a) is replaced by an MR that is only weakly hysteretic (again due to the PMA, which results in maximum coercive field for H perpendicular to the substrate [28,29]), also inverting in sign from positive for H parallel to I to negative for H perpendicular to I. This is the giant AMR effect previously reported in LSCO films [30], completely consistent with the metallic transport seen in Figs. 4(j)–4(l). The situation in Fig. 5(f) is thus implicated, where the electronically/magnetically phase-separated interfacial layer on this substrate is substantially thinner than the film thickness (60 Å), resulting in an "overlayer" with long-range F order and metallicity. The behavior in $SrTiO_3$(110)/LSCO in Fig. 5(b) is intermediate between that in Figs. 5(a) and 5(c). Specifically, the MR with H perpendicular to I remains negative and hysteretic, while the data with H parallel to I show a positive low-field effect (AMR) competing with a negative high-field effect (intercluster MR), balancing to close to zero at 9 T [49]. This competition suggests the situation in Fig. 5(e), where this thickness (60 Å) is close to, but just above t^* on this substrate, leading to barely percolated transport. These conclusions are reinforced by Fig. S3 in Supplemental Material [48], which shows analogous MR data at a lower t of 35−40 Å (∼9-10 u.c.) on both $SrTiO_3$(110) and $LaAlO_3$(001). In the $LaAlO_3$(001)/LSCO case, pure AMR persists, consistent with the metallic transport in Fig. 4(l). On $SrTiO_3$(110), on the other hand, the AMR and intercluster MR effects again compete, this time with a stronger intercluster MR component, consistent with the crossover toward weakly insulating transport in Figs. 4(g) and 4(h). In the ultrathin limit, $LaAlO_3$(001)/LSCO films thus outperform $SrTiO_3$(110)/LSCO (*i.e.*, they have lower t^* and t_d), both having greatly enhanced electronic/magnetic properties relative to $SrTiO_3$(001)/LSCO.

Discussion and Summary. Together, the data of Figs. 2–5 provide a consistent picture of the thickness-dependent electronic and magnetic properties of LSCO films, as a function of heteroepitaxial strain and growth orientation. On $SrTiO_3$(001), strong suppression of F order and metallicity occurs below a $t^* \approx 70$ Å (18 u.c.), due to an inhomogeneous, electronically and magnetically phase-separated, interfacial layer. These deleterious effects are significantly mitigated on $SrTiO_3$(110), which transitions to insulating transport only at 30 Å (8 u.c.) thickness. This mitigation is yet more effective under mild compressive strain on $LaAlO_3$(001), where 8-unit-cell-thick films exhibit metallic transport with ∼0.2 mΩ cm residual resistivity and F order with $T_C \approx 175$ K. Dead layer effects resulting from interfacial electronic/magnetic phase separation are thus

highly sensitive to both the sign of the heteroepitaxial strain and the growth orientation in LSCO. STEM-EELS and PNR chemical/magnetic depth profiling data provide essential context for these findings, establishing that epitaxial strain and orientation not only precisely control the V_O order in LSCO films, but also the depth profile of the interconnected V_O density and strain [38], which in turn control electronic and magnetic properties. These results provide important insight into the interplay between lattice mismatch, strain, defect ordering, and electronic/magnetic behavior in LSCO films, enabling optimization of properties even in the ultrathin-film limit. Given the interest in LSCO films in contexts as diverse as electronic, magnetic, and thermal properties [9,10,22–30,37,38,47,49,50,54,55], photonics [11], mixed ionic/electronic conduction [12], solid oxide fuel cells [13,14], and catalysis [15], this is of broad relevance.

Acknowledgments. This work was primarily supported by the US Department of Energy through the University of Minnesota (UMN) Center for Quantum Materials, under Grant No. DE-SC0016371. Parts of this work were conducted in the UMN Characterization Facility, which is partially supported by the National Science Foundation through the MRSEC program under DMR-2011401. STEM-EELS measurements were carried out in the former STEM group at Oak Ridge National Laboratory, supported by the U.S. Department of Energy, Office of Science, Basic Energy Sciences, Materials Sciences and Engineering Division. Work at Los Alamos National Laboratory (LANL) was supported by Basic Energy Sciences, US Department of Energy, under grant DE FG03-87ER-45332. LANL is operated by LANL LLC under DOE Contract DE-AC52-06NA25396. This research also used resources at the Spallation Neutron Source, a Department of Energy Office of Science User Facility operated by Oak Ridge National Laboratory. Work at nanoGUNE was supported by the Spanish Ministry of Science and Innovation under the Maria de Maeztu Units of Excellence Program (Grant No. CEX2020-001038-M) and Project No. PID2021-123943NB-I00 (OPTOMETAMAG). UMN authors acknowledge productive discussions with Javier Garcia Barriocanal.

This manuscript was authored in part by UT-Battelle, LLC, under Contract No. DE6AC0500OR22725 with the U.S. Department of Energy. The U.S. Government is authorized to reproduce and distribute reprints for Government purposes notwithstanding any copyright notation hereon. The Department of Energy will provide public access to these results of federally sponsored research in accordance with the DOE Public Access Plan.

Data Availability. The data that support the findings of this article are openly available [56].

[1] R. Ramesh and D. G. Schlom, Whither oxide electronics? MRS Bull. **33**, 1006 (2008).

[2] H. Y. Hwang, Y. Iwasa, M. Kawasaki, B. Keimer, N. Nagaosa, and Y. Tokura, Emergent phenomena at oxide interfaces, Nat. Mater. **11**, 103 (2012).

[3] J. H. Ngai, F. J. Walker, and C. H. Ahn, Correlated oxide physics and electronics, Annu. Rev. Mater. Res. **44**, 1 (2014).

[4] A. Bhattacharya and S. J. May, Magnetic oxide heterostructures, Annu. Rev. Mater. Res. **44**, 65 (2014).

[5] F. Hellman, A. Hoffmann, Y. Tserkovnyak, G. S. D. Beach, E. E. Fullerton, C. Leighton, A. H. MacDonald, D. C. Ralph, D. A. Arena, H. A. Dürr, P. Fischer, J. Grollier, J. P. Heremans, T. Jungwirth, A. V Kimel, B. Koopmans, I. N. Krivorotov, S. J. May, A. K. Petford-Long, J. M. Rondinelli, N. Samarth, I. K. Schuller, A. N. Slavin, M. D. Stiles, O. Tchernyshyov, A. Thiaville, and B. L. Zink, Interface-induced phenomena in magnetism, Rev. Mod. Phys. **89**, 025006 (2017).

[6] F. Gunkel, D. V. Christensen, Y. Z. Chen, and N. Pryds, Oxygen vacancies: The (in)visible friend of oxide electronics, Appl. Phys. Lett. **116**, 120505 (2020).

[7] M. A. Senaris-Rodriguez and J. B. Goodenough, Magnetic and transport properties of the system $La_{1-x}Sr_xCoO_{3-\delta}$ ($0 < x < 0.50$), J. Sol. Stat. Chem. **118**, 323 (1995).

[8] J. Wu and C. Leighton, Glassy ferromagnetism and magnetic phase separation in $La_{1-x}Sr_xCoO_3$, Phys. Rev. B **67**, 174408 (2003).

[9] Q. Lu *et al.*, Bi-directional tuning of thermal transport in $SrCoO_x$ with electrochemically induced phase transitions, Nat. Mater. **19**, 655 (2020).

[10] Y. Zhang, W. M. Postiglione, R. Xie, C. Zhang, V. Chaturvedi, K. Heltemes, H. Zhou, T. Feng, C. Leighton, and X. Wang, Wide-range continuous tuning of the thermal conductivity of $La_{1-x}Sr_xCoO_{3-\delta}$ films via room-temperature ion-gel gating, Nat. Commun. **14**, 2626 (2023).

[11] R. D. Chakraborty, W. M. Postiglione, S. Ghosh, K. A. Mkhoyan, C. Leighton, and V. E. Ferry, Electrochemically gated $La_{1-x}Sr_xCoO_{3-\delta}$ as a voltage-tunable phase-change material for infrared active metasurfaces, Adv. Opt. Mater. **11**, 2300098 (2023).

[12] Y-I. Kwon, G. D. Nam, G. Lee, S. Choi, and J. H. Joo, Recent progress and challenges in mixed ionic–electronic conducting membranes for oxygen separation, Adv. Energy Sustainability Res. **3**, 2200086 (2022).

[13] Edited by T. Ishihara, *Perovskite Oxide for Solid Oxide Fuel Cells* (Springer, New York, 2009).

[14] A. Samreen, M. S. Ali, M. Huzaifa, N. Ali, B. Hassan, F. Ullah, S. Ali, and N. A. Asrifin, Advancements in perovskite-based cathode materials for solid oxide fuel cells: A comprehensive review, Chem. Rec. **24**, e202300247 (2024).

[15] M. A. Pena and J. L. G. Fierro, Chemical structures and performance of perovskite oxides, Chem. Rev. **101**, 1981 (2001).

[16] S. Yamaguchi, Y. Okimoto, H. Taniguchi, and Y. Tokura, Spin-state transition and high-spin polarons in $LaCoO_3$, Phys. Rev. B **53**, R2926 (1996).

[17] A. Podlesnyak, M. Russina, A. Furrer, A. Alfonsov, E. Vavilova, V. Kataev, B. Büchner, T. Strässle, E. Pomjakushina, K. Conder, and D. I. Khomskii, Spin-state polarons in lightly-hole-doped $LaCoO_3$, Phys. Rev. Lett. **101**, 247603 (2008).

[18] P. P. Orth, D. Phelan, J. Zhao, H. Zheng, J. F. Mitchell, C. Leighton, and R. M. Fernandes, The essential role of magnetic frustration in the phase diagrams of doped cobaltites, Phys. Rev. Mater. **6**, L071402 (2022).

[19] D. Phelan, D. Louca, S. Rosenkranz, S.-H. Lee, Y. Qiu, P. J. Chupas, R. Osborn, H. Zheng, J. F. Mitchell, J. R. D. Copley, J. L. Sarrao, and Y. Moritomo, Nanomagnetic droplets and implications to orbital ordering in $La_{1-x}Sr_xCoO_3$, Phys. Rev. Lett. **96**, 027201 (2006).

[20] J. Wu, J. W. Lynn, C. Glinka, J. Burley, H. Zheng, J. F. Mitchell, and C. Leighton, Inter-granular giant magnetoresistance in a spontaneously phase separated perovskite oxide, Phys. Rev. Lett. **94**, 037201 (2005).

[21] C. He, S. El-Khatib, J. Wu, J. W. Lynn, H. Zheng, J. F. Mitchell, and C. Leighton, Doping fluctuation-driven magneto-electronic phase separation in $La_{1-x}Sr_xCoO_3$ single crystals, Europhys. Lett. **87**, 27006 (2009).

[22] D. Fuchs, C. Pinta, T. Schwarz, P. Schweiss, P. Nagel, S. Schuppler, R. Schneider, M. Merz, G. Roth, and H. v. Löhneysen, Ferromagnetic order in epitaxially strained $LaCoO_3$ thin films, Phys. Rev. B **75**, 144402 (2007).

[23] N. Biškup, J. Salafranca, V. Mehta, M. P. Oxley, Y. Suzuki, S. J. Pennycook, S. T. Pantelides, and M. Varela, Insulating ferromagnetic $LaCoO_{3-\delta}$ films: A phase induced by ordering of oxygen vacancies, Phys. Rev. Lett. **112**, 087202 (2014).

[24] W. S. Choi, J.-H. Kwon, H. Jeen, J. E. Hamann-Borrero, A. Radi, S. Macke, R. Sutarto, F. He, G. A. Sawatzky, V. Hinkov, M. Kim, and H. N. Lee, Strain-induced spin states in atomically ordered cobaltites, Nano Lett. **12**, 4966 (2012).

[25] J. Fujioka, Y. Yamasaki, H. Nakao, R. Kumai, Y. Murakami, M. Nakamura, M. Kawasaki, and Y. Tokura, Spin-orbital superstructure in strained ferrimagnetic perovskite cobalt oxide, Phys. Rev. Lett. **111**, 027206 (2013).

[26] E.-J. Guo, R. Desautels, D. Lee, M. A. Roldan, Z. Liao, T. Charlton, H. Ambaye, J. Molaison, R. Boehler, D. Keavney, A. Herklotz, T. Z. Ward, H. N. Lee, and M. R. Fitzsimmons, Exploiting symmetry mismatch to control magnetism in a ferroelastic heterostructure, Phys. Rev. Lett. **122**, 187202 (2019).

[27] V. Chaturvedi, J. Walter, A. Paul, A. Grutter, B. Kirby, J. S. Jeong, B. Yu, Z. Zhang, H. Zhou, M. Greven, K. A. Mkhoyan, T. Birol, and C. Leighton, Strain-induced majority carrier inversion in ferromagnetic epitaxial $LaCoO_{3-\delta}$ thin films, Phys. Rev. Mater. **4**, 034403 (2020).

[28] J. Walter, M. Cabero Piris, G. Yu, M. Greven, M. Varela, and C. Leighton, Perpendicular magnetic anisotropy via strain-engineered oxygen vacancy ordering in epitaxial $La_{1-x}Sr_xCoO_{3-\delta}$, Phys. Rev. Mater. **2**, 111404(R) (2018).

[29] S. Hu, C. Cazorla, F. Xiang, H. Ma, J. Wang, J. Wang, X. Wang, C. Ulrich, L. Chen, and J. Seidel, Strain control of giant magnetic anisotropy in metallic perovskite $SrCoO_{3-\delta}$ thin films, ACS Appl. Mater. Interf. **10**, 22348 (2018).

[30] J. Walter, S. Bose, M. Cabero, M. Varela, and C. Leighton, Giant anisotropic magnetoresistance in oxygen-vacancy-ordered epitaxial $La_{0.5}Sr_{0.5}CoO_{3-\delta}$ films, Phys. Rev. Mater. **4**, 091401(R) (2020).

[31] Y. Takeda, R. Kanno, T. Takada, O. Yamamoto, M. Takano, and Y. Bando, Phase relation and oxygen-non-stoichiometry of perovskite-like compound $SrCoO_x$ ($2.29 < x < 2.80$), Z. Anorg. Allg. Chem. **540**, 259 (1986).

[32] A. Nemudry, P. Rudolf, and R. Schöllhorn, Topotactic electrochemical reactions of the defect perovskite $SrCoO_{2.5+x}$, Chem. Mater. **8**, 2232 (1996).

[33] Y. Ito, R. F. Klie, N. D. Browning, and T. J. Mazanec, Atomic reolution analysis of the defect chemistry and microdomain structure of brownmillerite-type strontium cobaltite, J. Am. Ceram. Soc. **85**, 969 (2004).

[34] R. Le Toquin, W. Paulus, A. Cousson, C. Prestipino, and C. Lamberti, Time-resolved in-situ studies of oxygen intercalation into $SrCoO_{2.5}$, performed by neutron diffraction and X-ray absorption spectroscopy, J. Am. Chem. Soc. **128**, 13161 (2006).

[35] A. Muñoz, C. de la Calle, J. A. Alonso, P. M. Botta, V. Pardo, D. Baldomir, and J. Rivas, Crystallographic and magnetic structure of brownmillerite: Neutron study coupled with band-structure calculations, Phys. Rev. B **78**, 054404 (2008).

[36] C. K. Xie, Y. F. Nie, B. O. Wells, J. I. Budnick, W. A. Hines, and B. Dabrowski, Magnetic phase separation in $SrCoO_x$ ($2.5 < x < 3$), Appl. Phys. Lett. **99**, 052503 (2011).

[37] D. O. Klenov, W. Donner, B. Foran, and S. Stemmer, Impact of stress on oxygen vacancy ordering in epitaxial $(La_{0.5}Sr_{0.5})CoO_{3-\delta}$, Appl. Phys. Lett. **82**, 3427 (2003).

[38] J. Gazquez, S. Bose, M. Sharma, M. A. Torija, S. J. Pennycook, C. Leighton, and M. Varela, Lattice mismatch accommodation via oxygen vacancy ordering in epitaxial $La_{0.5}Sr_{0.5}CoO_3$ thin films, APL Mater. **1**, 012105 (2013).

[39] M. Bibes, L. Balcells, S. Valencia, J. Fontcuberta, M. Wojcik, E. Jedryka, and S. Nadolski, Nanoscale multiphase separation at $La_{2/3}Ca_{1/3}MnO_3/SrTiO_3$ interfaces, Phys. Rev. Lett. **87**, 067210 (2001).

[40] M. Huijben, L. W. Martin, Y.-H. Chu, M. B. Holcomb, P. Yu, G. Rijnders, D. H. A. Blank, and R. Ramesh, Critical thickness and orbital ordering in ultrathin $La_{0.7}Sr_{0.3}MnO_3$ films, Phys. Rev. B **78**, 094413 (2008).

[41] R. Herger, P. R. Wilmott, C. M. Schleputz, M. Bjorck, S. A. Pauli, D. Martoccia, B. D. Paterson, D. Kumah, R. Clarke, Y. Yacoby, and M. Dobeli, Structure determination of monolayer-by-monolayer grown $La_{1-x}Sr_xMnO_3$ thin films and the onset of magnetoresistance, Phys. Rev. B **77**, 085401 (2008).

[42] A. M. Kane, I.-T. Chiu, N. J. Ahlm, R. V. Chopdekar, A. T. N'Diaye, E. Arenholz, A. Mehta, V. Lauter, and Y. Takamura, Controlling magnetization vector depth profiles of $La_{0.7}Sr_{0.3}CoO_3/La_{0.7}Sr_{0.3}MnO_3$ exchange spring bilayers via interface reconstruction, ACS Appl. Mater. Interf. **12**, 45437 (2020).

[43] B. Li, R. V. Chopdekar, A. M. Kane, K. Hoke, A. T. N'Diaye, E. Arenholz, and Y. Takamura, Thickness-dependent magnetic and electrical transport properties of epitaxial $La_{0.7}Sr_{0.3}CoO_3$ films, AIP Advances **7**, 045003 (2017).

[44] Z. Liao, F. Li, P. Gao, L. Li, J. Guo, X. Pan, R. Jin, E. W. Plummer, and J. Zhang, Origin of the metal-insulator transition in ultrathin films of $La_{2/3}Sr_{1/3}MnO_3$, Phys. Rev. B **92**, 125123 (2015).

[45] E.-J. Guo, M. A. Roldan, T. Charlton, Z. Liao, Q. Zheng, H. Ambaye, A. Herklotz, Z. Gai, T. Z. Ward, H. N. Lee, and M. R. Fitzsimmons, Removal of the magnetic dead layer by geometric design, Adv. Func. Mater. **28**, 1800922 (2018).

[46] B. Ye, B. Liu, Y. Yin, H. Zhang, Y. Zhu, Z. Zhu, W. Liao, W. Gao, H. Guo, X. Zhou, W. Wang, C. Zheng, L. Yin, Y. Zhu, H. Xiang, and J. Shen, Reducing the magnetic dead layer to one unit cell in ultrathin films of manganites using spin-orbit coupling, Phys. Rev. B **108**, 094406 (2023).

[47] M. A. Torija, M. Sharma, J. Gazquez, M. Varela, C. He, J. Schmitt, J. A. Borchers, M. Laver, S. El-Khatib, and C. Leighton, Chemically-driven nanoscopic magnetic phase separation at the $SrTiO_3(001)/La_{1-x}Sr_xCoO_3$ interface, Adv. Mater. **23**, 2711 (2011).

[48] See Supplemental Material at http://link.aps.org/supplemental/10.1103/PhysRevMaterials.9.L031402 for additional information and data on: Experimental and analysis methods, X-ray diffraction characterization, PNR refinements, and magnetoresistance measurements.

[49] M. A. Torija, M. Sharma, M. R. Fitzsimmons, M. Varela, J. Wu, and C. Leighton, Epitaxial $La_{0.5}Sr_{0.5}CoO_3$ thin films: Structure, magnetism and transport, J. Appl. Phys. **104**, 023901 (2008).

[50] J. Gazquez, W. Luo, M. P. Oxley, M. Prange, M. A. Torija, M. Sharma, C. Leighton, S. T. Pantiledes, S. J. Pennycook, and M. Varela, Atomic resolution imaging of spin-state superlattices in nanopockets within cobaltite thin films, Nano Lett. **11**, 973 (2011).

[51] G. Campillo, A. Berger, J. Osorio, J. E. Pearson, S. D. Bader, E. Baca, and P. Prieto, Substrate dependence of magnetic properties of $La_{0.67}Ca_{0.33}MnO_3$ films, J. Mag. Mag. Mater. **237**, 61 (2001).

[52] A. Berger, G. Campillo, P. Vivas, J. E. Pearson, S. D. Bader, E. Baca, and P. Prieto, Critical exponents of inhomogeneous ferromagnets, J. Appl. Phys. **91**, 8393 (2002).

[53] A. Glavic and M. Bjorck, GenX 3: The latest generation of an established tool, J. Appl. Cryst. **55**, 1063 (2022).

[54] J. Walter, G. Yu, B. Yu, A. Grutter, B. Kirby, J. Borchers, Z. Zhang, H. Zhou, T. Birol, M. Greven, and C. Leighton, Ion-gel-gating-induced oxygen vacancy formation in epitaxial $La_{0.5}Sr_{0.5}CoO_{3-\delta}$ films from in operando x-ray and neutron scattering, Phys. Rev. Mater. **1**, 071403(R) (2017).

[55] M. Sharma, J. Gazquez, M. Varela, J. Schmitt, and C. Leighton, Coercivity enhancement driven by interfacial magnetic phase separation in $SrTiO_3(001)/Nd_{0.5}Sr_{0.5}CoO_3$, Phys. Rev. B **84**, 024417 (2011).

[56] C. Leighton, S. Bose, M. Sharma, M. A. Torija, J. Walter, N. Nandakumaran, J. Dewey, J. Schmitt, J. Gazquez, M. Varela, M. Zhernenkov, M. R. Fitzsimmons, H. Ambaye, V. Lauter, O. Hovoka, and A. Berger, "Controlling magnetism and transport at perovskite cobaltite interfaces via strain-tuned oxygen vacancy ordering (2025)", https://hdl.handle.net/11299/270214.